reactions

MDPI

Article

UV-Light-Driven Photocatalytic CO_2 Reduction over a Niobium-Based Metal–Organic Gel

Eduardo Abreu [1], Onelia A. A. dos Santos [1], Maria E. K. Fuziki [2], Marcio V. Zwierzykowski [2], Aline Coqueiro [3], Angelo M. Tusset [4], Michel Z. Fidelis [5] and Giane G. Lenzi [2,*]

[1] Department of Chemical Engineering, State University of Maringá, Avenida Colombo, 5790, Maringá 87020-900, Paraná, Brazil; eduardo_abreu@live.com (E.A.); oaasantos@uem.br (O.A.A.d.S.)
[2] Department of Chemical Engineering, Federal University of Technology–Paraná, R. Doutor Washington Subtil Chueire, 330-Jardim Carvalho, Ponta Grossa 84017-220, Paraná, Brazil; mariafuziki@utfpr.edu.br (M.E.K.F.); marcioz@alunos.utfpr.edu.br (M.V.Z.)
[3] Department of Chemistry, Federal University of Technology–Paraná, R. Doutor Washington Subtil Chueire, 330-Jardim Carvalho, Ponta Grossa 84017-220, Paraná, Brazil; alinedqi@utfpr.edu.br
[4] Department of Production Engineering, Federal University of Technology–Paraná, R. Doutor Washington Subtil Chueire, 330-Jardim Carvalho, Ponta Grossa 84017-220, Paraná, Brazil; tusset@utfpr.edu.br
[5] São Carlos Institute of Chemistry, University of São Paulo (USP), São Carlos 13566-590, São Paulo, Brazil; michelmzzf@usp.br
* Correspondence: gianeg@utfpr.edu.br

Abstract

The photocatalytic conversion of carbon dioxide (CO_2) into methanol represents a promising strategy for both greenhouse gas mitigation and renewable fuel production. In this study, a niobium-based metal–organic gel (Nb-MOG) was employed as a photocatalyst for the reduction of CO_2 to methanol under UV irradiation in a batch photoreactor. A two-factor experimental design was conducted to evaluate the effects of sodium carbonate concentration and catalyst loading on methanol production. The Nb-MOG catalyst was dispersed in the reaction medium and irradiated with UV light for four hours. During the photocatalytic experiments, samples were periodically collected and analyzed by headspace gas chromatography coupled with flame ionization detection (HS-GC-FID) to quantify methanol production. The results showed that both the Na_2CO_3 concentration and catalyst loading exerted significant positive effects on methanol formation. The highest methanol yield was achieved at a Na_2CO_3 concentration of 0.10 mol·L^{-1} and a catalyst loading of 0.50 g·L^{-1}. The experimental design results demonstrated a good fit of the statistical model to the experimental data, highlighting its predictive capability and confirming the reliability of the obtained results. Furthermore, Nb-MOG exhibited enhanced light-harvesting and charge-transfer properties, leading to measurable methanol production under the investigated conditions. These findings contribute to a better understanding of Nb-MOG's photocatalytic behavior and demonstrate its potential for application in a sustainable CO_2 reduction system.

Keywords: MOG; methanol production; sodium carbonate influence

Academic Editor: Hugo de Lasa

Received: 12 May 2026
Revised: 25 June 2026
Accepted: 2 July 2026
Published: 9 July 2026

1. Introduction

The rising levels of atmospheric carbon dioxide (CO_2) represent one of the most significant environmental challenges, directly linked to global warming and climate change [1]. The development of sustainable fuels capable of mitigating this problem is a central strategy in the energy transition. For example, converting CO_2 into value-added compounds, such

as methanol, not only reduces emissions but also enables the production of renewable fuels or chemical intermediates [1,2]. Recent overviews detail multiple pathways, photocatalytic, electrochemical, and thermocatalytic, for converting CO_2 into methanol, showing their potential for carbon mitigation with energy production [2].

It is important to note that CO_2 reduction can be carried out in both the liquid and gas phases [3]. In the liquid-phase reaction, CO_2 reduction is performed in an aqueous solution saturated with CO_2. However, the limited solubility of CO_2 in water represents a critical challenge for achieving efficient photocatalytic CO_2 reduction. Nevertheless, the solubility of CO_2 in water can be enhanced by the use of additives such as NaOH, $NaHCO_3$, or Na_2CO_3. These additives increase CO_2 solubility; however, reducing bicarbonate and carbonate species is more difficult [4].

CO_2 is thermodynamically stable and kinetically inert, but side reactions often reduce selectivity. In addition, achieving efficient light absorption, charge separation, and catalyst stability under reaction conditions is difficult [5,6].

Several parameters influence the photocatalytic reduction of CO_2, including the composition and structure of the photocatalyst, its morphology, the exposed crystal facets, particle size, surface vacancies, and the operating conditions (pH, pressure, temperature, and reducing agent) [4]. An increase in pH enhances the reaction rate.

Metal–Organic Frameworks (MOFs) are promising materials for CO_2 capture and catalytic conversion. MOFs are porous materials, built from metal centers and organic linkers, offering high surface areas and modular functionalization options [7,8]. Their structure allows a good link between adsorbed CO_2 molecules and catalytic sites, and the framework can be built to provide the desired electronic properties and light absorption [9,10]. Some recent reviews have specifically highlighted progress in functionalized MOFs for photocatalytic CO_2 reduction and strategies to overcome stability and recombination challenges [7,11]. Recent studies have reported interesting results on the application of MOFs and MOF-derived materials in CO_2 reduction. Wu et al. [12] reported the use of a MOF@COF hybrid material in CO_2 reduction, where COF means Covalent Organic Framework. The authors achieved a CH_4 yield rate of 21.27 μmol g^{-1} h^{-1}. Zhang et al. [13], in turn, achieved a CO production rate of 263.63 μmol g^{-1} h^{-1} using a 2D MOF/COF heterojunction. Liu et al. [14] prepared a MOF-on-MOF-derived $CuO@In_2O_3$ material, reaching 190.32 μmol g^{-1} h^{-1} and 500.46 μmol g^{-1} h^{-1} production rates for CH_4 and CO, respectively. Another MOF-on-MOF-derived material (Co_3O_4/In_2O_3) was reported by Han [15] and applied to CO_2 reduction, resulting in a CO yield of 4828 ± 570 μmol h^{-1} g^{-1}.

Despite the use of MOFs, a significant challenge lies in overcoming their poor macroformability and low hydrostability, which hinder their application as industrial adsorbents and catalysts. In this context, metal–organic gels (MOGs) have been reported as a promising alternative to MOFs. The morphology and chemical characteristics of an amorphous framework have been demonstrated to be advantageous for electrocatalytic carbon dioxide (CO_2) reduction [16]. These characteristics include larger pores that accommodate most of the confined fluid phase, with porous networks interconnected with semi-fluid or flexible structures that facilitate faster analyte diffusion, easier functionalization, and better processability in films, coatings, and monoliths [17]. These characteristics are particularly advantageous for gas separation processes, where efficient adsorption and desorption are essential. Furthermore, another application within the same context, already reported in the literature, is the synthesis and characterization of metal–organic gels for CO_2 capture applications [18].

Moreover, amorphous materials are metastable, and the structural disorder in their framework results in a higher density of active sites during electrochemical testing, such as in supercapacitor applications [19].

Despite its promising characteristics, reports of MOG's applications remain scarce. A Co/Fe-Metal–Organic Xerogel was described by Yang et al. [20], achieving a CO yield of 67 μmol g^{-1} h^{-1}. Verma et al. [21] prepared a Metal–Organic "Soft" Coordination Polymer Gel. They applied it to the photoreduction of CO_2 to CO, yielding 3.5 mmol g^{-1} h^{-1}, and to the conversion of CO_2 to CH_4, yielding 6.7 mmol g^{-1} h^{-1}, under the studied conditions. Furthermore, promising results were reported for visible-light-driven processes. For example, a Ti(VI)-based Metal–Organic Aerogel (MOA) described by Angulo-Ibáñez et al. [22] achieved a 221–786 μmol·g^{-1}·h^{-1} yield of methanol from CO_2 under visible-light irradiation. An MOA modified with copper (II)-metalated porphyrin was synthesized and applied by Perfecto-Irigaray et al. [23] in visible-light-driven conversion of CO_2 to alcohols (methanol and ethanol), up to a production rate of 356–642 μmol·g^{-1}·h^{-1}.

In this study, niobium is employed as the metal center in the synthesis of metal–organic gels (MOGs) and applied to CO_2 reduction, representing an unprecedented strategy according to the literature surveyed. Niobium pentoxide has emerged as a transition-metal oxide of significant scientific and technological interest due to its physicochemical properties, including chemical and thermal stability, corrosion resistance, and low toxicity [24]. A niobium-based metal–organic gel (MOG) derived from the MIL-125 (Ti-based) framework was investigated for the photocatalytic reduction of CO_2 to methanol.

2. Materials and Methods

2.1. Chemicals

All reagents used were of analytical grade, including sodium carbonate (Na_2CO_3, Synth, São Paulo, Brazil), dimethylformamide (DMF, Synth), methanol for GC (Sigma-Aldrich, Taufkirchen, Germany), 2-aminoterephthalic acid (Sigma-Aldrich, Germany), isopropyl alcohol P.A. A.C.S. 99.5% (Synth, Brazil), and niobium pentachloride ($NbCl_5$, Companhia Brasileira de Metalurgia e Mineração—CBMM, Araxá, Brazil). CO_2 gas with 99.9% purity was supplied by White Martins (Araucária, Brazil). Deionized water was used in all solution preparations.

2.2. Catalyst Synthesis

The Nb-MOG was synthesized by adapting the procedure originally proposed for MIL-125-NH_2 [25]. Niobium isopropoxide was prepared in situ through a reaction between $NbCl_5$ and isopropyl alcohol under an inert atmosphere. The procedure was carried out at a molar ratio of 1:5 ($NbCl_5$–isopropanol) under constant stirring for 60 min to ensure complete dissolution of the salt, as described by Castro et al. [26]. Subsequently, 0.35 mmol of niobium isopropoxide and 0.98 mmol of 2-aminoterephthalic acid were mixed in a solvent system composed of 8 mL of DMF and 2 mL of methanol. The resulting mixture was transferred to a Schlenk flask immersed in a glycerin bath and maintained at 373 K for 72 h. The obtained solid was washed sequentially with DMF and methanol and then dried at 70 °C for 12 h.

2.3. Catalyst Characterization

The catalyst used in this work was previously characterized by [27], using the following techniques: Scanning Electron Microscopy–Energy Dispersive X-ray Spectroscopy (SEM–EDS): Analysis was performed using VEGA3 TESCAN equipment (SEM/EDS, TESCAN, microscope model VEGA3, Brno, Czech Republic). Point zero charge (PZC) determination: The determination of the point of zero charge was performed using the method known as the "11-point experiment". The procedure consists of mixing 50 mg of the catalyst in 50 mL of aqueous solution under 11 different initial pH conditions (2, 3, 4, 5, 6, 7, 8, 9, 10, 11, and 12), adjusted with solutions of HCl or NaOH 0.1 mol·L^{-1}, and measuring the pH

after 24 h [28]. Fourier Transform Infrared Spectroscopy (FTIR): The spectra were obtained using a Perkin Elmer Frontier instrument (Beaconsfield, Buckinghamshire, UK) in the wavenumber range of 4000 to 400 cm^{-1}, with a resolution of 1 cm^{-1} and 32 accumulations. X-ray diffraction (XRD): Analysis of the samples was performed using a Rigaku MiniFlex 600 diffractometer (Rigaku Corporation, Tokyo, Japan), 40 kV and 15 mA, with Cu Kα radiation (λ = 1.5406 Å), at a scan interval of 2θ = 3–90°, in step scan mode, with a step of 0.02° and a time per step of 2 s. Thermogravimetric analysis (TG): Curves were obtained using a simultaneous thermal analysis system, model SDT 2960, from TA Instruments (SDT 2960, TA Instruments, New Castle, DE, USA). The analysis was performed under a flow of dry air or nitrogen at 100 mL min^{-1} and a heating rate of 10 °C min^{-1}. Diffuse Reflectance Spectroscopy (DRS): The band gap was obtained on a Varian Cary 500 Scan spectrophotometer (UV-VIS-NIR Spectrophotometer, Palo Alto, CA, USA).

2.4. CO_2 Reduction Tests

The tests were performed in a batch borosilicate glass photoreactor with a capacity of 1000 mL, equipped with a water-cooled jacket to maintain the reaction temperature near 290 K, in a photocatalytic chamber. A 250 W Hg vapor lamp was used as the radiation source (light intensity 13.55 $mW \cdot cm^{-2}$). Initially, an aqueous solution of sodium carbonate was prepared at a known concentration. CO_2 was continuously bubbled through the solution for 1 h at constant flow to ensure complete saturation (Figure 1). After this period, a known mass of the Nb-MOG catalyst (indicated in Table 1) was added, and the system was stirred under irradiation. During the experiments, variations in the catalyst and sodium carbonate concentrations were studied to determine the optimal conditions for converting CO_2 to methanol. The reaction proceeded for four hours, and 8 mL aliquots were collected every hour. For analysis, 3 mL of each withdrawn aliquot was first filtered through a 0.22 µm syringe filter to remove suspended catalyst particles. Then, 5 mL of the filtered sample was transferred into 20 mL headspace vials and sealed with aluminum/silicone septa.

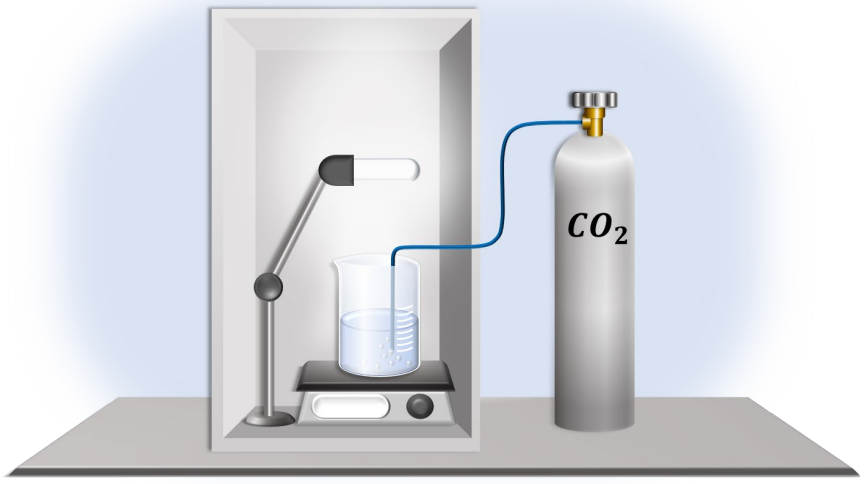

Figure 1. Schematic illustration of the CO_2 photoreduction reaction system.

Table 1. Results of the experimental design.

Run	Factors		Responses	
	Na_2CO_3 Conc. ($mol \cdot L^{-1}$)	Catalyst Concentration ($g \cdot L^{-1}$)	* Methanol (ppm)	Methanol ($\mu mol \cdot gcat^{-1} \cdot h^{-1}$)
1	0.010	0.100	4.32	1.59
2	0.010	0.300	19.65	2.42
3	0.010	0.500	56.67	4.19
4	0.055	0.100	7.16	2.64
5	0.055	0.300	51.22	6.32
6	0.055	0.500	90.52	6.70
7	0.100	0.100	48.84	18.07
8	0.100	0.300	95.51	11.78
9	0.100	0.500	189.20	14.01

* Concentration in the reaction solution.

2.5. Methanol Quantification

The method was based on the work of Ndikumana et al. [29]. Before injection, the vials were equilibrated at 100 °C for 10 min. The samples were analyzed using a gas chromatograph (YL Clarity, Anyang-si, Gyeonggi-do, Republic of Korea) equipped with a headspace autosampler and a flame ionization detector (FID). Headspace sampling was performed using an HTA HT200H autosampler configured with a 2 mL sample volume and a 1 s equilibration delay before injection. One injection was performed per vial. The autosampler oven, syringe, and transfer line were maintained at 100 °C. Electrovalve flushing was carried out for 2 min to prevent carryover. GC analysis was performed on a YL 6000 Series GC (GC, Yongin-si, Gyeonggi-do, Republic of Korea) equipped with a capillary column of 30 m × 0.25 mm × 0.25 µm. The injector operated in split mode at a 1:10 split ratio, with a split flow of 18 $mL \cdot min^{-1}$ and a total flow of 23 $mL \cdot min^{-1}$. The injector temperature was set to 250 °C. The oven program was as follows: initial temperature of 30 °C with 2.5 min hold, followed by a ramp of 60 $°C \cdot min^{-1}$ to 380 °C with a final 2.0 min hold, resulting in a total run time of approximately 6.7 min. The FID operated at 250 °C, with airflow at 400 $mL \cdot min^{-1}$, hydrogen at 40 $mL \cdot min^{-1}$, and makeup gas (N_2) at 10 $mL \cdot min^{-1}$. The detector range was set to 10,000 mV with a sampling rate of 10 Hz. Chromatographic peaks were integrated according to standard FID integration parameters, and methanol concentrations were determined from calibration curves (see Appendix A Calibration Curve) constructed from external standards treated under the same headspace conditions.

3. Results

3.1. Nb-MOG Catalyst

The Nb-MOG catalyst was characterized in detail by Abreu et al. (2026) [27]. The X-ray diffractogram indicates that the synthesized Nb-MOG exhibited a broad diffraction band centered between 20° and 35° (2θ), indicating its predominantly amorphous nature (Figure 2a). The absence of sharp diffraction peaks suggests a low degree of crystallinity, which is commonly observed in non-calcined materials. A weak diffraction feature around 27° (2θ) may indicate the presence of small crystalline domains embedded within the amorphous matrix. The morphology is characterized by a wrinkled, non-porous surface, similar to that observed in catalysts prepared by the chemical mixing method (sol–gel), a characteristic commonly reported in the literature for sol–gel-derived materials (Figure 2b). MOGs are described as an additional class of larger pores that accommodate most of the

solvent phase [3]. Energy Dispersive X-ray Spectroscopy (EDS) revealed a significant amount of niobium (Figure 2c), chlorine (Figure 2d), and oxygen (Figure 2e) on the surface. At the same time, the EDS spectrum indicated Nb, Cl, and O contents of 47.7%, 41.4%, and 10.9%, respectively (Figure 2e).

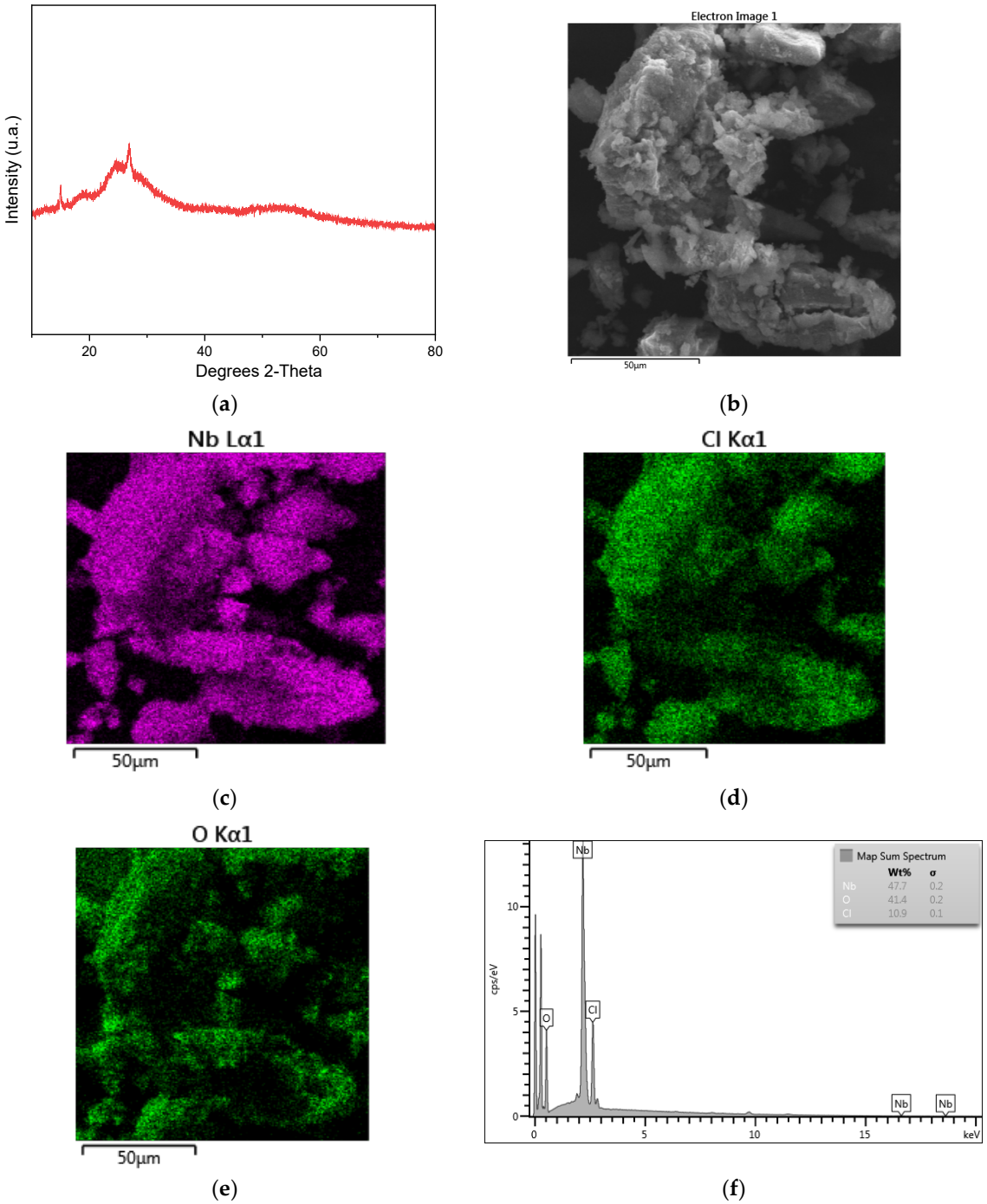

Figure 2. (**a**) X-ray diffraction; (**b**) SEM micrograph; (**c**) EDS elemental mapping of Nb (Nb Lα1); (**d**) EDS elemental mapping of Cl (Cl Kα1); (**e**) EDS elemental mapping of O (O Kα1); and (**f**) EDS spectrum showing the elemental composition of the sample.

The band gap energy of Nb-MOG was estimated to be 1.88 eV using photoacoustic spectroscopy (Figure 3a). The point of zero charge (PZC) was determined to be 4.6 (Figure 3b). The infrared spectrum shows characteristic bands of amorphous niobium oxide (Figure 4a).

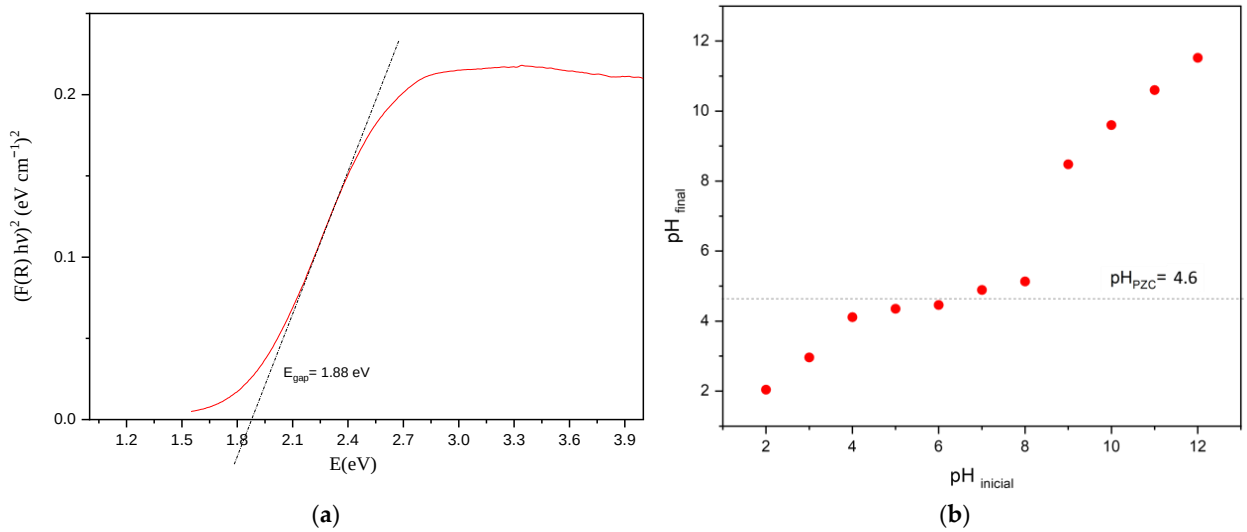

(**a**) (**b**)

Figure 3. Characterization results: (**a**) band gap and (**b**) PCZ.

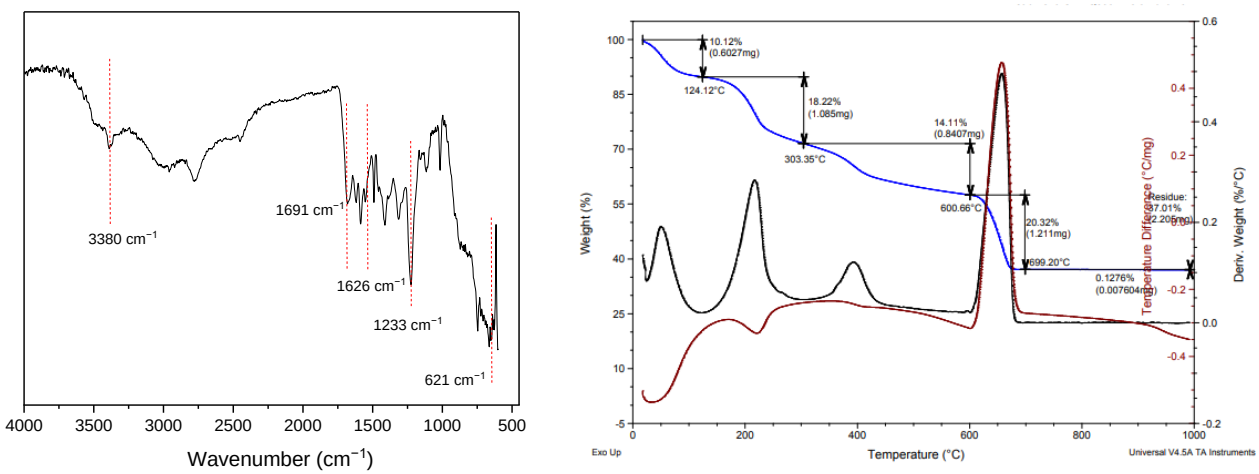

(**a**) (**b**)

Figure 4. Characterization results: (**a**) Infrared spectra and (**b**) TGA/DTGA profile.

Figure 4a shows the FTIR spectrum of the Nb-MOG sample, which exhibits absorption bands characteristic of amorphous niobium oxide. Other studies have reported that a band near 621 cm^{-1} is indicative of amorphous niobium oxide materials. The absorption observed around 850 cm^{-1} can be attributed to the symmetric stretching vibration of the Nb–O bonds. The bands at approximately 1626 and 3380 cm^{-1} are attributed to bending and stretching vibrations of hydroxyl groups and water molecules adsorbed on the material's surface, respectively [30]. The band detected at 1233 cm^{-1} corresponds to the stretching vibration of the C–NH_2 group. This attribution is consistent with the theoretical and experimental FTIR analyses reported by Karabacak et al. (2010), who associated this absorption with amino group vibrations coupled to aromatic ring modes [31].

The thermogravimetric analysis (TG) (Figure 4b) reveals a multi-stage mass-loss profile, typical of metal–organic gels (Figure 4b). In the first stage, a mass loss of 10.12% was observed below 124 °C, attributed to the removal of adsorbed water and solvent molecules from the gel. In the second stage, the most significant mass loss of 18.22% occurred between 124 and 303 °C, resulting from the release of strongly retained solvent and the partial decomposition of organic components. Subsequently, a gradual mass loss of 14.11% occurred from 303 to 600 °C, resulting from the progressive decomposition of

organic binders and the disruption of metal–ligand interactions. Finally, a major mass loss of 20.32% occurred between 600 and 700 °C, associated with the combustion of residual carbonaceous species and the formation of the metal oxide.

3.2. Experimental Design Results

A two-factor experimental design was established to evaluate the influence of the sodium carbonate concentration and catalyst loading on the photocatalytic conversion of CO_2 to methanol. The factors and their respective levels were defined as follows: Na_2CO_3 concentration at 0.010, 0.055, and 0.100 mol·L^{-1}, and catalyst concentration at 0.1, 0.3, and 0.5 g·L^{-1}. A full factorial arrangement (3^2) was employed, resulting in nine experimental runs, each corresponding to a unique combination of the two variables. This design allowed the systematic assessment of both the individual effects of each factor and their potential interaction on methanol production. Table 1 summarizes all experiments conducted during the final 4 h of methanol production, and Figure 5 presents the kinetic curves for CO_2 photoreduction (MeOH (ppm) vs. time (h)). The amount of methanol formed, under the experimental conditions studied, is directly influenced by the amounts of catalyst and Na_2CO_3. All experiments indicated that the greater the catalyst amount, the greater the methanol production. The same trend occurred for Na_2CO_3. This behavior can be explained by the number of available active sites and the solubility of CO_2 in water. The literature describes CO_2 as having limited solubility in water, which is a problem for the effectiveness of the reduction process using a saturated aqueous solution of CO_2. However, the solubility of CO_2 in aqueous medium can be improved with the use of additives such as NaOH, $NaHCO_2$, or Na_2CO_2 [4]. These additives increase the solubility of CO_2, although reducing bicarbonate and carbonate species is more difficult. In this sense, Tseng et al. observed that an alkaline medium was beneficial in the photoreduction of CO_2. They observed a substantial increase in the rate of methanol formation with the addition of NaOH, which they attributed to two factors: (1) the strong hole-capturing capacity of OH^- ions in aqueous solution, which helps to reduce the electron–hole recombination rate and maximizes the lifetime of free electrons, and (2) the greater solubility of CO_2 in aqueous NaOH solution than in pure water [32].

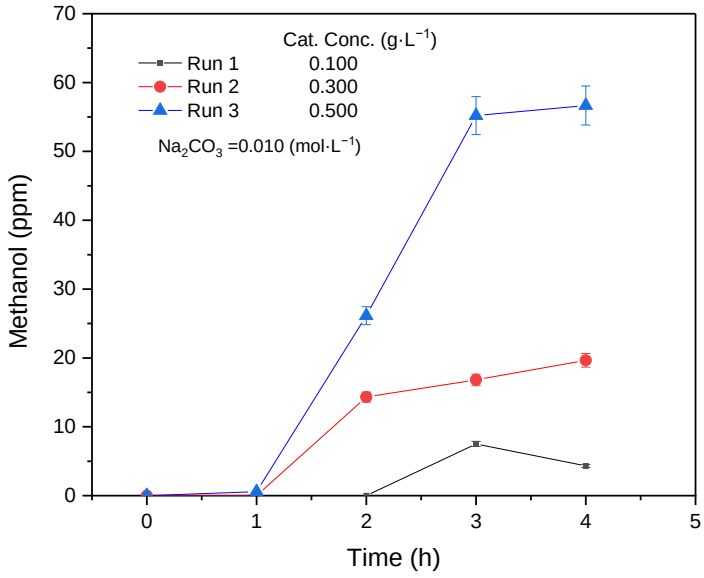

Figure 5. *Cont.*

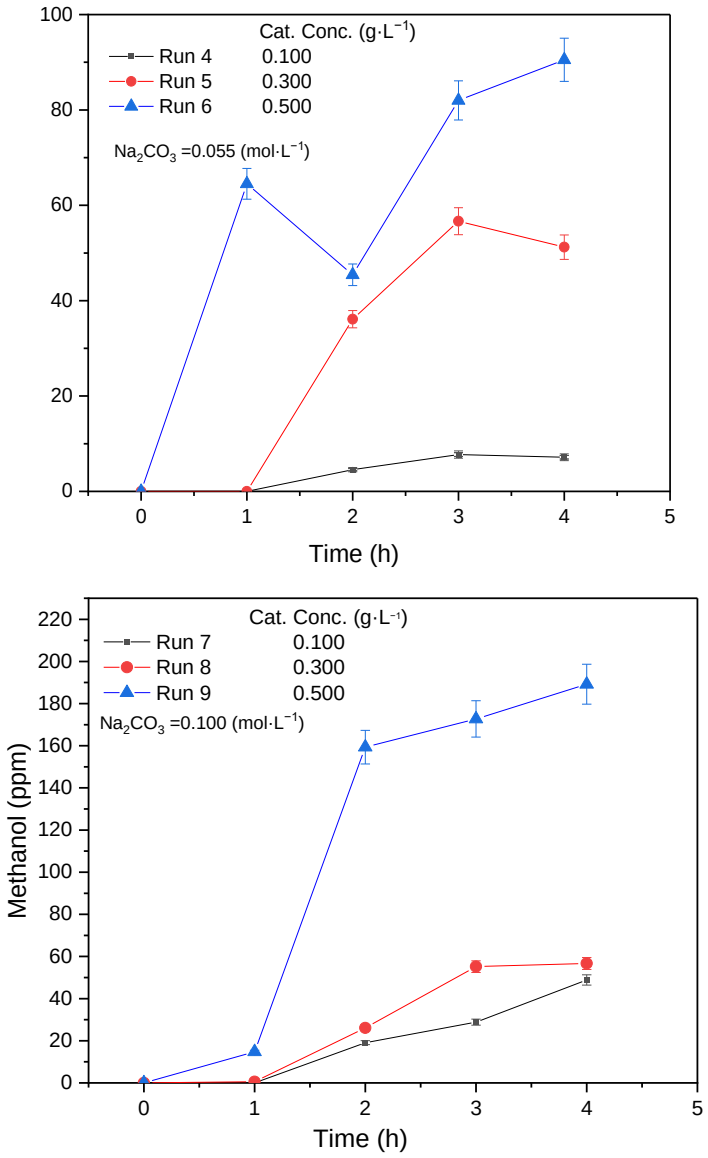

Figure 5. Methanol amount vs. time.

Figure 6 a and b show the fitted surface plots and response surface, respectively, for the experimental design, and Figure 7 shows the observed vs. predicted values.

The ANOVA shows that the model adequately describes the experimental data (Table 2), with R^2 = 0.9257 and an adjusted R^2 of 0.8513, indicating that most of the variability in methanol production is explained by the fitted quadratic model. Among the evaluated factors, the linear effect of sodium carbonate concentration was statistically significant (p = 0.0097), confirming that increasing the Na_2CO_3 concentration positively influenced methanol formation. The linear effect of catalyst concentration was also significant (p = 0.0373), indicating that the catalyst loading contributed to the enhancement of the photocatalytic conversion.

Quadratic terms for both variables were included in the model to account for curvature in the response surface. However, neither the quadratic effect of Na_2CO_3 (p = 0.2843) nor that of catalyst concentration (p = 0.5900) reached statistical significance at the 95% confidence level. This suggests that, within the studied range, the primary contribution to methanol production arises predominantly from the linear increase in both factors rather than strong curvature in their individual effects.

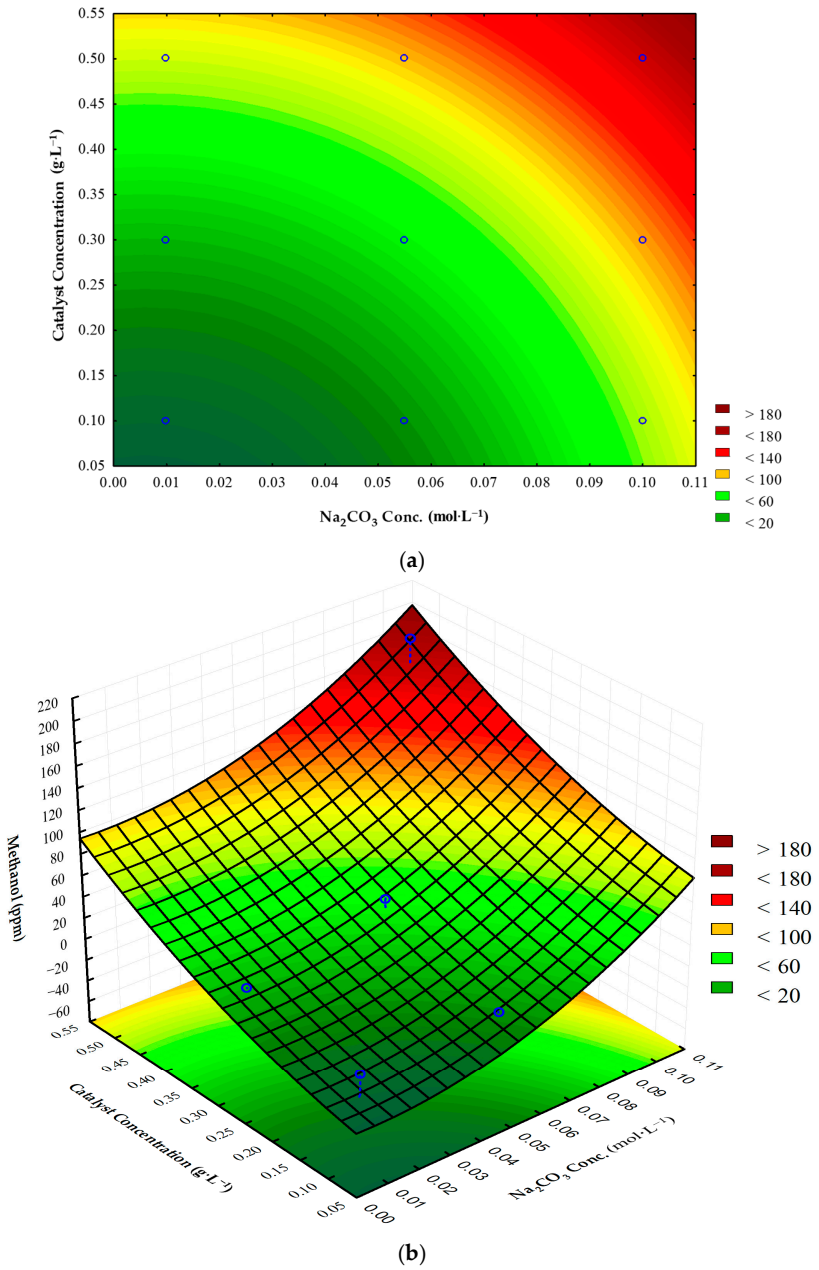

Figure 6. (**a**) Contour plots and (**b**) response surface for the experimental design. Blue points represent the experimental data.

Overall, the ANOVA confirms that both sodium carbonate concentration and catalyst loading exert significant linear effects on methanol production, and the response surface indicates that higher levels of both factors favor greater methanol production.

The agreement between the experimental and model-predicted methanol concentrations was evaluated using an observed-versus-predicted plot (Figure 3). The data points were distributed closely around the diagonal reference line, indicating that the quadratic model adequately represented the experimental system. No systematic deviations were observed, such as curvature, clustering, or bias toward over- or under-prediction, confirming the fit within the studied domain.

The results obtained in the present work reveal a clear and consistent positive effect of both Na_2CO_3 concentration and catalyst loading on the photocatalytic production of methanol. Under the most favorable conditions tested (0.10 mol·L^{-1} Na_2CO_3 and 0.50 g·L^{-1} of the Nb-MOG catalyst), the system produced 189.20 ppm of methanol

(≈14.01 μmol·gcat^{-1}·h^{-1} over four hours). These values demonstrate that, even in a simple aqueous carbonate medium and without the use of sacrificial agents or noble-metal cocatalysts, the system is capable of generating quantifiable amounts of methanol, a relevant result considering that many photocatalytic CO_2 reduction studies report only trace or negligible methanol under comparable conditions.

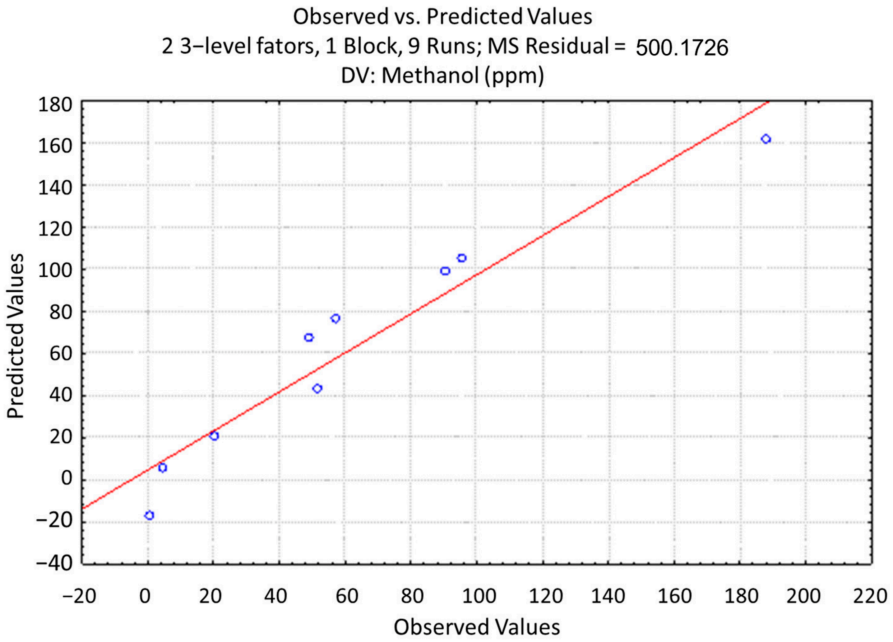

Figure 7. Observed vs. predicted values.

Table 2. ANOVA results from the experimental design.

Source	SS [a]	df [b]	MS [c]	F [d]	*p* [e]
(1) Na_2CO_3 Conc. (mol/L) (L)	10,817.96	1	10,817.96	21.62845	0.009657
Na_2CO_3 Conc. (mol/L) (Q)	763.23	1	763.23	1.52594	0.284318
(2) Catalyst Conc. (g/L) (L)	4716.33	1	4716.33	9.42940	0.037266
Catalyst Conc. (g/L) (Q)	171.13	1	171.13	0.34213	0.590006
Error	2000.69	4	500.17		
Total SS	26,907.55	8			

[a] quadratic effect; [b] degrees of freedom; [c] mean square; [d] F-value; [e] probability value.

When placed in the context of the recent literature, the performance achieved here is modest in terms of rate per mass of catalyst. Still, it remains notable given the simplicity of the catalytic system. For instance, metal-decorated MOF systems frequently exhibit higher methanol productivities: Cu SAs/UiO-66-NH_2 has been reported to reach 5.33 μmol·g^{-1}·h^{-1} [33], and Zn_2GeO_4/ZIF-67 produces 5.18 μmol·g^{-1}·h^{-1} [34]. More sophisticated catalysts, such as Ni/Zr-CU-BDC, can reach even higher values, such as 41.05 μmol·g^{-1}·h [35]. The study by Elsafi et al. [36], which describes MOF-based photocatalysts (ZIF-8 decorated with metal nanoparticles such as Au or Cu), reported methanol production rates that are significantly higher (up to 2650 μmol·gcat^{-1}·h^{-1} for Au/ZIF-8 under UV–visible irradiation).

Nevertheless, these literature examples typically rely on noble metals, advanced engineered structures, sacrificial electron donors, or non-aqueous media, which strongly enhance charge separation and CO_2 activation. In contrast, the present study demonstrates that significant methanol accumulation can be achieved in a purely aqueous carbonate environment using a single Nb-MOG photocatalyst. These results highlight the system's

potential as a simpler, more sustainable alternative, even if its productivity per gram of catalyst remains lower than that of highly engineered materials.

The experimental and model-predicted methanol concentrations exhibit minimal dispersion, indicating that the model closely tracks the experimental data. This behavior reinforces the regression model's reliability in describing the effects of sodium carbonate and catalyst concentrations on methanol formation.

Regarding the pathway for CO_2 reduction to methanol, a plausible literature-based reaction mechanism is proposed in Figure 8, based on the works [37–39], to provide a conceptual interpretation of the photocatalytic process. Although control experiments such as dark, catalyst-free, and CO_2-free tests were not performed in this study, the photocatalytic mechanism proposed herein is consistent with the current understanding of CO_2 photoreduction, which requires light-induced charge carriers for CO_2 activation and conversion.

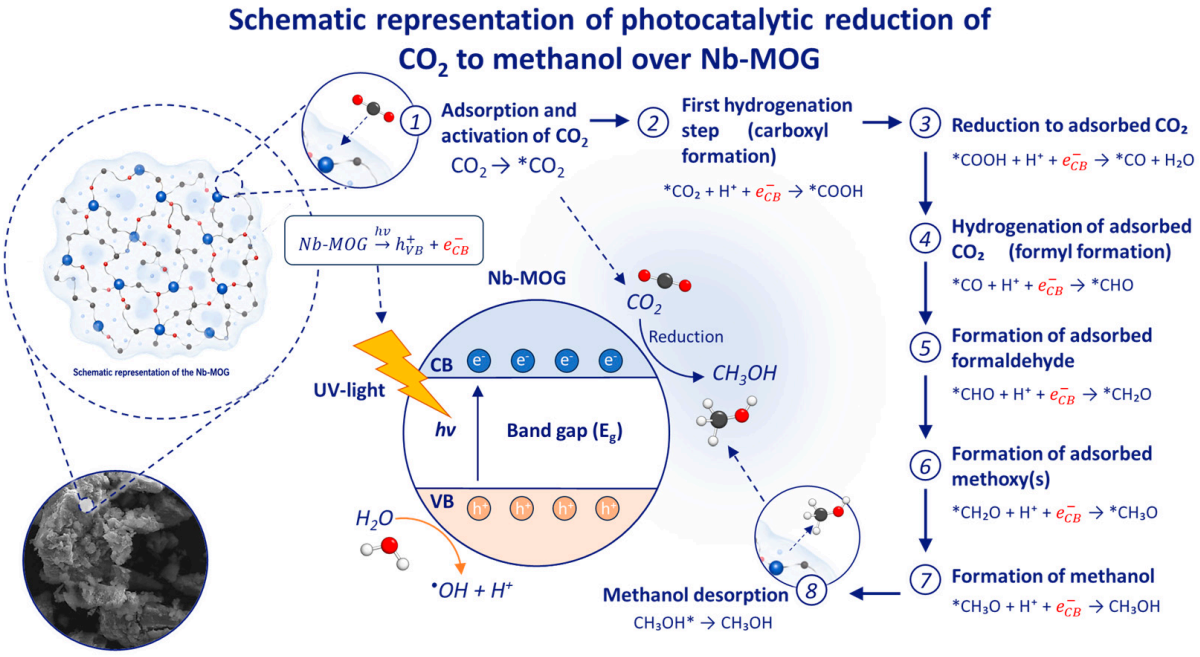

Figure 8. Suggested reaction mechanism for the photoreduction of CO_2 to generate methanol.

Chen et al. [3] conducted control and isotope experiments using $^{13}CO_2$. They confirmed that the CO originated from the photocatalytic reduction of CO_2. The same study found that the apparent quantum yield (AQY) of the $TiO_2/BiVO_4$-4 catalyst decreased with increasing irradiation wavelength, suggesting that photogenerated carriers were primarily responsible for CO production. A possible explanation is that slower electron transport met the two-electron requirement, yielding a single product: CO.

4. Conclusions

This study demonstrates that an Nb-MOG-based photocatalyst can promote the reduction and recycling of CO_2 into methanol in a simple aqueous carbonate medium. Both sodium carbonate concentration and catalyst loading showed significant positive linear effects on methanol production, with the highest yield obtained at 0.10 mol·L^{-1} Na_2CO_3 and 0.50 g·L^{-1} catalyst loading. It was observed that adding Na_2CO_3 increased the solubility of CO_2 in water, thereby influencing process performance. Furthermore, a higher concentration of the Nb-MOG catalyst led to a greater number of active sites, thereby increasing the amount of methanol. The statistical model adequately described the system, confirming the reliability of the experimental results.

Although the methanol production rate of the proposed photocatalyst is lower than that reported for advanced MOF-based photocatalysts using noble metals or sacrificial agents, its performance is notable given the system's simplicity and the absence of co-catalysts or sacrificial donors. These findings highlight the potential of Nb-MOG as a sustainable and low-complexity material for photocatalytic CO_2 valorization and provide a basis for further optimization.

Author Contributions: Conceptualization, E.A., G.G.L. and M.E.K.F.; methodology, A.C., E.A., M.Z.F. and O.A.A.d.S.; validation, A.M.T. and M.Z.F.; formal analysis, G.G.L. and M.E.K.F.; investigation, O.A.A.d.S. and M.V.Z.; writing—original draft preparation, E.A., A.C.; writing—review and editing, A.C., G.G.L., O.A.A.d.S., M.Z.F., A.M.T. and M.E.K.F.; supervision, O.A.A.d.S. All authors have read and agreed to the published version of the manuscript.

Funding: This research was funded by the Conselho Nacional de Desenvolvimento Científico e Tecnológico (CNPq), grant PQ Process No. 304068/2022-5, and by the Programa Ibero-Americano de Ciencia y Tecnología para el Desarrollo (CYTED) through the project CATPROH2.

Data Availability Statement: The data used to support the findings of this study are included within the article.

Acknowledgments: The authors thank the Capes, Fundação Araucaria, and CNPq, as well as LabMult C2MMa-UTFPR-Ponta Grossa for providing access to their laboratories to perform the analyses.

Conflicts of Interest: The authors declare no conflicts of interest.

Appendix A

Calibration Curve

The calibration curve for methanol quantification was prepared using GC-grade methanol. Six standard solutions were prepared by transferring 5 mL of aqueous solutions containing 167, 333, 667, 1000, 1333, and 1667 ppm of methanol into 20 mL headspace vials, which were then sealed with aluminum/silicone septa. All standards were analyzed under the same headspace and chromatographic conditions used for the samples, ensuring full methodological equivalence between calibration and analytical runs. The results can be found in Table A1, and the curve in Figure A1.

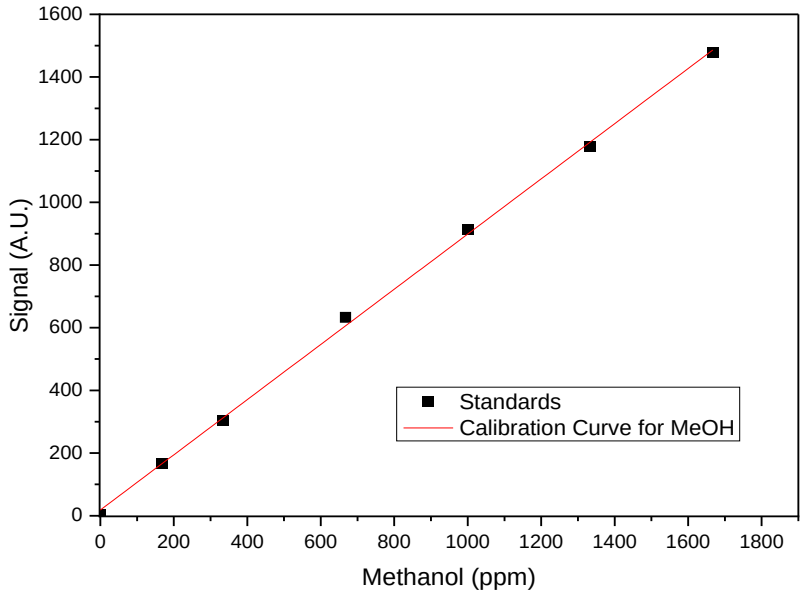

Figure A1. Calibration curve for methanol.

Table A1. Results from the calibration curve.

Methanol (ppm)	Signal (A.U)
0	4.3
167	165.3
333	304.6
667	633.4
1000	912.6
1333	1179.3
1667	1478.5

The calibration curve for methanol showed excellent linearity over the evaluated concentration range, with a linear regression equation of $y = 0.88058x + 18.29363$ and a correlation coefficient (R^2) of 0.99905. The method showed adequate sensitivity, yielding a limit of detection (LOD) of 12.6 ppm and a limit of quantification (LOQ) of 38.3 ppm, calculated from the standard deviation of the response and the slope of the calibration curve. Precision was evaluated in triplicate, yielding coefficients of variation (CVs) of 1.24% at 167 ppm, 0.97% at 667 ppm, and 1.19% at 1667 ppm, demonstrating good repeatability across the analytical range. The chromatograms are shown in Figure A2.

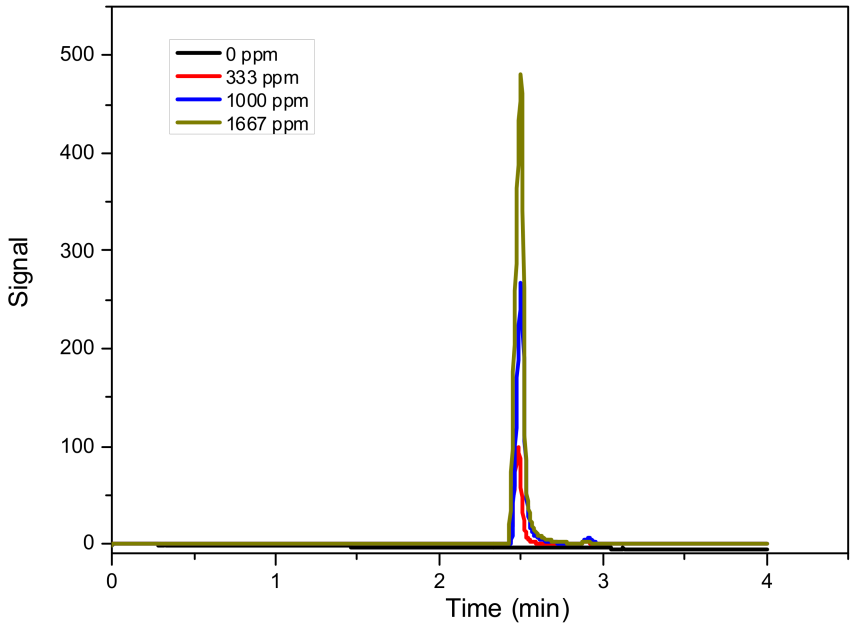

Figure A2. Chromatograms from the calibration curve.

References

1. Jiang, X.; Nie, X.; Guo, X.; Song, C.; Chen, J.G. Recent Advances in Carbon Dioxide Hydrogenation to Methanol via Heterogeneous Catalysis. *Chem. Rev.* **2020**, *120*, 7984–8034. [CrossRef] [PubMed]
2. Sajnani, S.; Memon, M.A.; Memon, S.A.; Kumar, A.; Mehvish, D.; Ameen, S.; Mukarama; Zhou, W.; Liu, Y. CO_2 to Methanol Conversion: A Bibliometric Analysis with Insights into Reaction Mechanisms, and Recent Advances in Catalytic Conversion. *Processes* **2025**, *13*, 314. [CrossRef]
3. Chen, C.; Wu, M.; Xu, Y.; Ma, C.; Song, M.; Jiang, G. Efficient Photoreduction of CO_2 to CO with 100% Selectivity by Slowing Down Electron Transport. *J. Am. Chem. Soc.* **2024**, *146*, 9163–9171. [CrossRef] [PubMed]
4. Lingampalli, S.R.; Ayyub, M.M.; Rao, C.N.R. Recent Progress in the Photocatalytic Reduction of Carbon Dioxide. *ACS Omega* **2017**, *2*, 2740–2748. [CrossRef] [PubMed]
5. Khalil, M.T.; Wu, X.; Liu, S.; Liu, Y.; Ashraf, S.; Shen, R.; Zhang, H.; Peng, Z.; Jiang, J.; Li, B. Recent advancements in catalytic CO_2 conversion to methanol: Strategies, innovations, and future directions. *Green Chem.* **2025**, *27*, 9016–9054. [CrossRef]

6. Ye, J.; Dimitratos, N.; Rossi, L.M.; Thonemann, N.; Beale, A.M.; Wojcieszak, R. Hydrogenation of CO_2 for sustainable fuel and chemical production. *Science* **2025**, *387*, eadn9388. [CrossRef] [PubMed]
7. Li, T.; Wang, P.; He, M.; Zhang, T.; Yang, C.; Li, Z. Metal-organic frameworks for photocatalytical carbon dioxide reduction reaction. *Coord. Chem. Rev.* **2024**, *521*, 216179. [CrossRef]
8. Zheng, J.; Yan, X.; Guo, X.; Wang, X.; Tang, S.; Liu, M. Advancements in Metal–Organic Framework Materials for Photocatalytic CO_2 Reduction. *Catalysts* **2025**, *15*, 208. [CrossRef]
9. Khan, M.; Akmal, Z.; Tayyab, M.; Mansoor, S.; Zeb, A.; Ye, Z.; Zhang, J.; Wu, S.; Wang, L. MOFs materials as photocatalysts for CO_2 reduction: Progress, challenges and perspectives. *Carbon Capture Sci. Technol.* **2024**, *11*, 100191. [CrossRef]
10. Huang, T.; Yang, H.; Xu, W.; Sun, Y.; Pang, H. Research progress of MOF-based materials in photocatalytic reduction of CO_2 and N_2. *Chem. Catal.* **2024**, *4*, 100929. [CrossRef]
11. Mori, R. CO_2 photocatalytic reduction with robust and stable metal–organic framework: A review. *Mater. Renew. Sustain. Energy* **2024**, *13*, 109–132. [CrossRef]
12. Wu, Z.; Li, W.; Hou, L.; Wei, Q.; Yang, H.; Jiang, Y.; Tang, D. A novel Sunflower-like MOF@COF for improved photocatalytic CO_2 reduction. *Sep. Purif. Technol.* **2023**, *311*, 123322. [CrossRef]
13. Zhang, N.; Sun, Y.; Liu, X.; Yin, R.; Wang, Y.; Wang, S.; Wei, J.; Zhang, G.; Dong, H.; Zhang, F. 2D MOF/COF Heterojunction for Efficient Photothermal Synergistic Catalysis of CO_2 Reduction. *Adv. Funct. Mater.* **2026**, *36*, e23743. [CrossRef]
14. Liu, X.; Wu, Y.; Li, Y.; Yang, X.; Ma, Q.; Luo, J. MOF-on-MOF-derived CuO@In_2O_3 s-scheme heterojunction with core–shell structure for efficient photocatalytic CO_2 reduction. *Chem. Eng. J.* **2024**, *485*, 149855. [CrossRef]
15. Han, C.; Zhang, X.; Huang, S.; Hu, Y.; Yang, Z.; Li, T.; Li, Q.; Qian, J. MOF-on-MOF-Derived Hollow Co_3O_4/In_2O_3 Nanostructure for Efficient Photocatalytic CO_2 Reduction. *Adv. Sci.* **2023**, *10*, e2300797. [CrossRef] [PubMed]
16. Santos-Lorenzo, J.; San José-Velado, R.; Albo, J.; Beobide, G.; Castaño, P.; Castillo, O.; Luque, A.; Pérez-Yáñez, S. A straightforward route to obtain zirconium based metal-organic gels. *Microporous Mesoporous Mater.* **2019**, *284*, 128–132. [CrossRef]
17. Bedair, A.; Algethami, F.K.; Alqarni, L.S.; Hamed, M.; Locatelli, M.; Mansour, F.R. Application of metal organic gels (MOGs) in analytical chemistry. *TrAC Trends Anal. Chem.* **2026**, *202*, 118939. [CrossRef]
18. Nune, S.K.; Thallapally, P.K.; McGrail, B.P. Metal organic gels (MOGs): A new class of sorbents for CO_2 separation applications. *J. Mater. Chem.* **2010**, *20*, 7623–7625. [CrossRef]
19. Yang, F.; Li, W.; Tang, B. Facile synthesis of amorphous UiO-66 (Zr-MOF) for supercapacitor application. *J. Alloys Compd.* **2018**, *733*, 8–14. [CrossRef]
20. Yang, K.; Chen, L.; Duan, X.; Song, G.; Sun, J.; Chen, A.; Xie, X. Ligand-controlled bimetallic Co/Fe MOF xerogels for CO_2 photocatalytic reduction. *Ceram. Int.* **2023**, *49*, 16061–16069. [CrossRef]
21. Verma, P.; Rahimi, F.A.; Samanta, D.; Kundu, A.; Dasgupta, J.; Maji, T.K. Visible-Light-Driven Photocatalytic CO_2 Reduction to CO/CH_4 Using a Metal–Organic "Soft" Coordination Polymer Gel. *Angew. Chem. Int. Ed.* **2022**, *61*, e202116094. [CrossRef] [PubMed]
22. Angulo-Ibáñez, A.; Perfecto-Irigaray, M.; Merino-Garcia, I.; Luengo, N.; Goitandia, A.M.; Albo, J.; Aranzabe, E.; Beobide, G.; Castillo, O.; Pérez-Yáñez, S. Metal-organic aerogels based on titanium(IV) for visible-light conducted CO_2 photoreduction to alcohols. *Mater. Today Energy* **2022**, *30*, 101178. [CrossRef]
23. Perfecto-Irigaray, M.; Merino-Garcia, I.; Albo, J.; Beobide, G.; Castillo, O.; Luque, A.; Pérez-Yáñez, S. Copper(II)-porphyrin functionalized titanium(IV) metal-organic aerogels for the visible-light driven conversion of CO_2 to alcohols. *Mater. Today Energy* **2023**, *36*, 101346. [CrossRef]
24. Khalid, M.U.; Rudokaite, A.; da Silva, A.M.H.; Kirsnyte-Snioke, M.; Stirke, A.; Melo, W.C.M.A. A Comprehensive Review of Niobium Nanoparticles: Synthesis, Characterization, Applications in Health Sciences, and Future Challenges. *Nanomaterials* **2025**, *15*, 106. [CrossRef] [PubMed]
25. Hendon, C.H.; Tiana, D.; Fontecave, M.; Sanchez, C.; D'arras, L.; Sassoye, C.; Rozes, L.; Mellot-Draznieks, C.; Walsh, A. Engineering the Optical Response of the Titanium-MIL-125 Metal–Organic Framework through Ligand Functionalization. *J. Am. Chem. Soc.* **2013**, *135*, 10942–10945. [CrossRef] [PubMed]
26. Castro, D.C.; Cavalcante, R.P.; Jorge, J.; Martines, M.A.U.; Oliveira, L.C.S.; Casagrande, G.A.; Machulek, A., Jr. Synthesis and Characterization of Mesoporous Nb_2O_5 and Its Application for Photocatalytic Degradation of the Herbicide Methylviologen. *J. Braz. Chem. Soc.* **2015**, *27*, 303–313. [CrossRef]
27. Abreu, E.; dos Santos, O.A.A.; Fuziki, M.E.K.; Tusset, A.M.; Fidelis, M.Z.; Motheo, A.J.; Lenzi, G.G. Nb-MOG as a High-Performance Photocatalyst for Cr(VI) Remediation: Optimization and Reuse Cycles. *Catalysts* **2026**, *16*, 60. [CrossRef]
28. Robles, J.; Regalbuto, J.R. The Engineering of Pt/Carbon Catalyst Preparation for Application on Proton Exchange Fuel Cell Membrane (PEFCM). 2004. Available online: https://api.semanticscholar.org/CorpusID:46982313 (accessed on 11 May 2026).
29. Ndikumana, E.; Niyonizera, E.; Kabera, J.; Pandey, A. Analysis of Methanol and Ethanol Content in Illegal Alcoholic Beverages using Headspace Gas Chromatography: Case Studies at Rwanda Forensic Institute. *Braz. J. Anal. Chem.* **2024**, *11*, 18–33. [CrossRef]

30. Cantão, F.d.O.; Melo, W.d.C.; Oliveira, L.C.A.; Passos, A.R.; da Silva, A.C. Utilization of Sn/Nb_2O_5 composite for the removal of methylene blue. *Quim. Nova* **2010**, *33*, 528–531. [CrossRef]
31. Karabacak, M.; Cinar, M.; Unal, Z.; Kurt, M. FT-IR, UV spectroscopic and DFT quantum chemical study on the molecular conformation, vibrational and electronic transitions of 2-aminoterephthalic acid. *J. Mol. Struct.* **2010**, *982*, 22–27. [CrossRef]
32. Tseng, I.H.; Chang, W.C.; Wu, J.C.S. Photoreduction of CO_2 using sol–gel derived titania and titania-supported copper catalysts. *Appl. Catal. B* **2002**, *37*, 37–48. [CrossRef]
33. Becerra, J.; Nguyen, D.T.; Gopalakrishnan, V.N.; Do, T.O. Plasmonic Au Nanoparticles Incorporated in the Zeolitic Imidazolate Framework (ZIF-67) for the Efficient Sunlight-Driven Photoreduction of CO_2. *ACS Appl. Energy Mater.* **2020**, *3*, 7659–7665. [CrossRef]
34. Wu, K.; Liu, C.; Chen, Y.; Jiang, H.; Peng, Q.; Chen, Y.; Fang, D.; Shen, B.; Wu, Q.; Zhan, L.; et al. Constructing asymmetric unsaturated copper coordination in Zinc(II)/Copper(I, II)-based metal-organic framework toward productive CO_2-to-methanol photocatalytic conversion from CO_2-capturing solution. *Appl. Catal. A Gen.* **2023**, *650*, 118970. [CrossRef]
35. Hu, M.; Liu, J.; Song, S.; Wang, W.; Yao, J.; Gong, Y.; Li, C.; Li, H.; Li, Y.; Yuan, X.; et al. Ultra-thin Two-Dimensional Trimetallic Metal–Organic Framework for Photocatalytic Reduction of CO_2. *ACS Catal.* **2022**, *12*, 3238–3248. [CrossRef]
36. Elsafi, A.; Theihmed, Z.; Al-Yafei, A.; Alkhateeb, A.; Abotaleb, A.; Anwar, M.; Mroue, K.; Aissa, B.; Sinopoli, A. Plasmon-Enhanced CO_2 Reduction to Liquid Fuel via Modified UiO-66 Photocatalysts. *Catalysts* **2025**, *15*, 70. [CrossRef]
37. Zhu, Z.; Xing, X.; Qi, Q.; Li, H.; Han, D.; Song, X.; Tang, X.; Ng, Y.H.; Huo, P. Regulation CN reduction of CO_2 products selectivity by adjusting the number of V sites and mechanism exploration. *Fuel* **2025**, *388*, 134509. [CrossRef]
38. Qi, Q.; Shen, W.; Yan, Y.; Fang, Y.; Zhang, Y.; Tang, X.; Huo, P. Construction of In-modified CN-based photocatalyst with In–N chemical bond for efficient photoreduction of CO_2. *J. Mater. Sci. Technol.* **2026**, *261*, 161–170. [CrossRef]
39. Shen, W.; Qi, Q.; Hu, B.; Zhu, Z.; Huo, P.; Jiang, J.; Tang, X. Studying bimetals copper-indium for enhancing PCN photocatalytic CO_2 reduction activity and selectivity mechanism. *J. Ind. Eng. Chem.* **2025**, *145*, 384–394. [CrossRef]